Journal of Biomedical Optics 16(7), 076004 (July 2011)

Qualitative near-infrared vascular imaging system with tuned aperture computed tomography

Tatsuhiko Matsushita,[a,b] Tosiaki Miyati,[a,b] Kazuya Nakayama,[a] Takashi Hamaguchi,[a,c] Yoshihiko Hayakawa,[d] Allan G. Farman,[e] and Shigeki Ohtake[a,b]
[a]Kanazawa University, Graduate School of Medical Science, Division of Health Science, 5-11-80 Kodatsuno, Kanazawa, 920-0942, Japan
[b]Kanazawa University, Institute of Medical, Pharmaceutical and Health Science, Wellness Promotion Science Center, 5-11-80 Kodatsuno, Kanazawa, 920-0942, Japan
[c]Kanazawa University Hospital, Department of Radiology, 13-1 Takara-machi, Kanazawa, 920-8641, Japan
[d]Kitami Institute of Technology, Department of Computer Science, Faculty of Engineering, 165 Koen-cho, Kitami, Hokkaido, 090-8507, Japan
[e]University of Louisville School of Dentistry, Division of Radiology and Imaging Science, Department of Surgical and Hospital Dentistry, Louisville, Kentucky 40292

Abstract. We developed a novel system for imaging and qualitatively analyzing the surface vessels using near-infrared (NIR) radiation using tuned aperture computed tomography (TACT®). The system consisted of a NIR-sensitive CCD camera surrounded by sixty light emitting diodes (with wavelengths alternating between 700 or 810 nm). This system produced thin NIR tomograms, under 0.5 mm in slice thickness. The venous oxygenation index reflecting oxygen saturation levels calculated from NIR tomograms was more sensitive than that from the NIR images. This novel system makes it possible to noninvasively obtain NIR tomograms and accurately analyze changes in oxygen saturation. *© 2011 Society of Photo-Optical Instrumentation Engineers (SPIE).* [DOI: 10.1117/1.3595424]

Keywords: near infrared; tuned aperture computed tomography; near infrared tomogram; venous oxygenation index.

Paper 10642PR received Dec. 8, 2010; revised manuscript received Apr. 6, 2011; accepted for publication May 9, 2011; published online Jul. 8, 2011.

1 Introduction

The regional vascular oxygenation level provides very important clinical information for the analysis of biological conditions. Vascular oxygenation levels need to be measured as an aid to monitor blood oxygen levels and saturation; therefore, noninvasive measurement methods under realistic biological conditions have been developed.[1–5] These are permitted by measurement method using near infrared (NIR). Systems described in the literature are based on a specific characteristic that NIR is absorbed by the hemoglobin in blood.[6] Additionally, development of noncontact sensing methods to define the location of the near surface veins holds considerable promise for aiding in obtaining blood samples from individuals whose veins are not evident from visual inspection.[7] Such capability would be especially useful for infants and those with elevated BMI values. Since NIR can transmit through thin regions such as through a finger, vascular images can be easily acquired[8,9] and monitoring blood oxygen saturation can be easily measured.[10] Although using a transmission method is limited to thin regions, this study developed a novel system for the noninvasive imaging of surface vessels in thick regions where NIR imaging is not always feasible. Additionally, NIR tomograms using tuned aperture computed tomography (TACT®) were obtained, as well as measurements of the regional vascular oxygenation levels.

Address all correspondence to: Tatsuhiko Matsushita, Kanazawa University, Graduate School of Medical Science, Division of Health Science, 5-11-80 Kodatsuno, Kanazawa, 920-0942, Japan; Tel: 81-76-2652500; Fax: 81-76-2344351; E-mail: tmatusi@mhs.mp.kanazawa-u.ac.jp.

In this paper, we demonstrated the utility of this system and described its characteristics and potential future in clinical applications.

2 Materials and Methods

2.1 *System*

A NIR-sensitive charged-coupled device (CCD) camera (XC-EI50/50CE, Sony Corporation, Tokyo, Japan) was surrounded by sixty light emitting diodes (LED) (alternating wavelengths between 700 to 810 nm, VSF706C1 and LSF811C1, Optrans, Tokyo, Japan), that could only detect NIR from subcutaneous tissues (Fig. 1). The NIR was absorbed across surface vessels more than any other surrounding tissues.

2.2 *Tuned Aperture Computed Tomography Theory*

TACT is a reconstruction method that can be used to synthesize three-dimensional representation from multiple arbitrary prerecorded two-dimensional basis images (each acquired at a different angle) of an interesting region. The basic principles of the TACT algorithm are derived from the optical aperture theory and tomosynthesis.[11,12] The TACT stacks the basis images, inputs locations of fiducial markers for each basis image, and reconstructs a series of arbitrary multiplanner cross-sectional images. Stability for maintaining continuity in geometric is required for the generation of three-dimensional images, such as computed tomography, at the time of collection of images. However, TACT enables an arbitrary setup of projection directions,

1083-3668/2011/16(7)/076004/5/$25.00 © 2011 SPIE

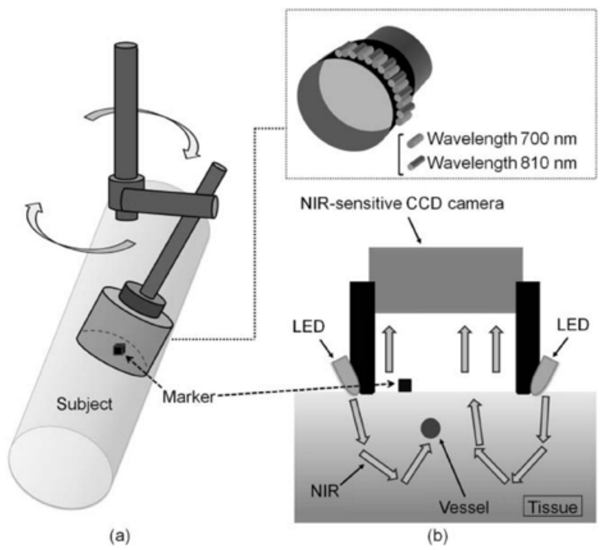

Fig. 1 (a) Acquisition system and (b) schematic diagram for NIR imaging.

because the position of the fiducial markers is always available. Moreover, because image reconstruction often involves only shifting and adding two-dimensional images, the process is rapidly and efficiently managed by even the simplest image-processing computers. Iterative restoration is often utilized in TACT imaging in an attempt to improve detailed clarity.[13,14] The iterative restoration algorithm works for the deblurring of TACT slices to remove out-of-focus noise. TACT has been used in the clinical application of digital mammography[15] and oral surgery using x-ray emitting devices,[16] whereas there has been no study, that we are aware of, that reconstructed NIR tomograms.

2.3 *Tomograms*

To increase the image contrast of the vessels and obtain three-dimensional information, we created tomograms calculated from NIR images (basis images) using the TACT program (TACT Workbench version 0.9.43). First, for the TACT series, a fiducial marker was used by attaching approximately 1 mm wire to the forearm skin within the field of view. Next, when considering the factors influencing the image accuracy of TACT,[17–19] six concentric NIR projections of surface vessels including the marker were obtained and reconstructed as tomograms (Fig. 2). The angular disparity was set at 30 deg during each projection. Reconstructed images were processed by using the proprietary iterative restoration algorithm three times (default setting).

2.4 *Venous Oxygenation Index*

Multiple NIR images (six projections in total) of surface vessels on the forearm were obtained before and after the loading test, that is, using a blood pressure cuff on the upper arm at each wavelength in accordance with the optical aperture theory[11,12] during the first second. We held the cuff pressure at more than 140 mmHg to occlude vessels. Then, tomograms were created using the TACT program and the venous oxygenation index (VOI) was calculated from the image signal intensities at each wavelength [Eq. (1)], which is an indicator of the oxygen

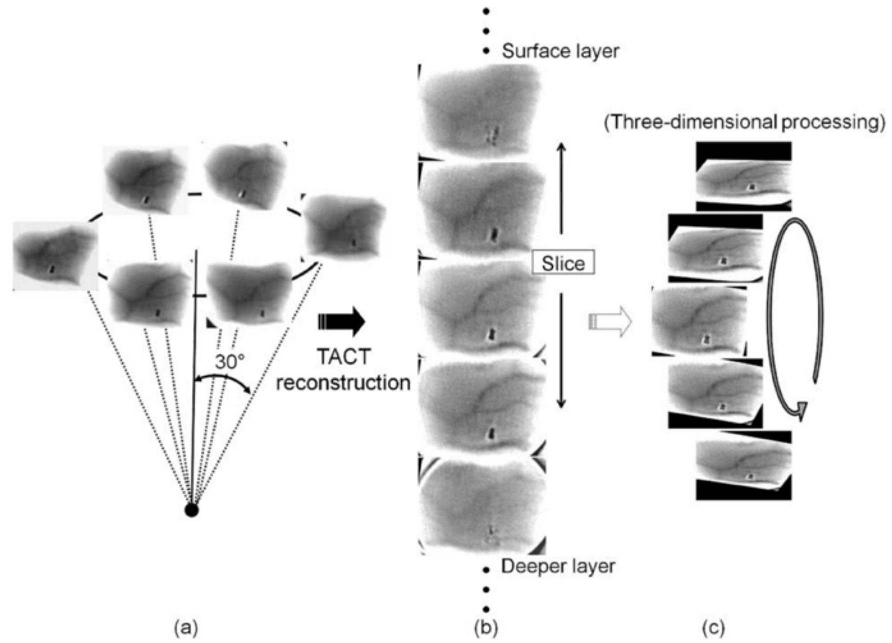

Fig. 2 One example for TACT procedure. (a) NIR images (wavelengths: 810 nm) of surface vessels and projection geometry relationships between angular disparity and numbers of projections performed. (b) TACT slices reconstructed from (a). (c) Rotated three-dimensional data structures from (b).

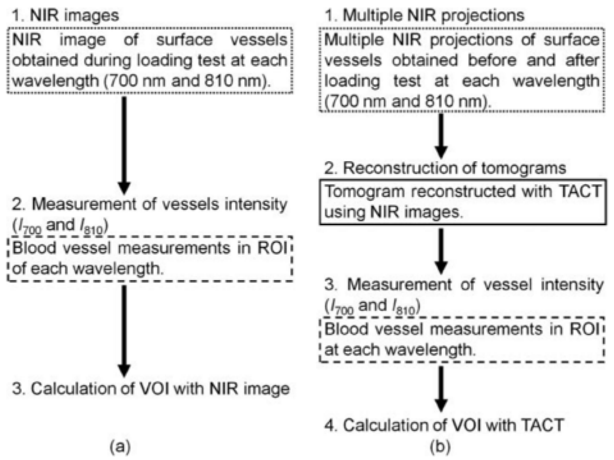

Fig. 3 VOI measurement procedures (a) without and (b) with tomograms.

saturation level,[20]

$$VOI = \frac{I_{700}}{I_{810}}, \tag{1}$$

where I_{700} and I_{810} are the signal intensities of the vessels for the 700 and 810 nm images, respectively. Figure 3 shows the measurement procedure for the calculation of VOI. Moreover, the VOI was compared to the oxygen saturation (SpO_2) using a pulse oximeter. The study was performed in five healthy volunteers after informed consent was obtained from each human subject.

2.5 *System Characteristics*

Correlation between the current supplied to the LED and the signal intensity of the NIR images was investigated, because signal intensity of a NIR image is relative value. When the current to the LED at each wavelength, respectively, was slowly increased to the maximum value, NIR images of LED light were obtained by CCD camera and the signal intensities of these images were measured.

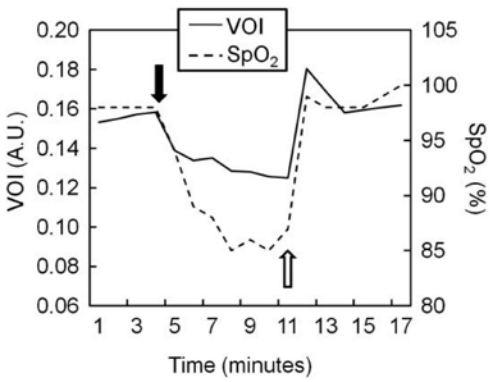

Fig. 4 Change in venous oxygenation index and SpO_2 during the loading test. Black arrow shows cuff pressure on and white arrow shows cuff pressure off. Note that there was good agreement with VOI and SpO_2. A.U.: arbitrary unit.

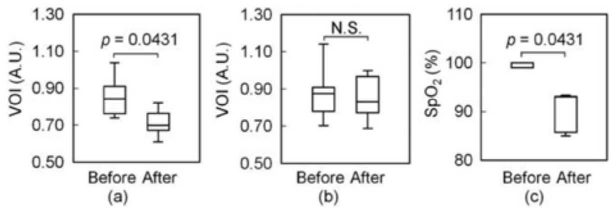

Fig. 5 Change in VOI (a) with and (b) without TACT, and (c) change in oxygen saturation (SpO_2) measured by pulse oximeter before and after loading test. VOI with TACT and SpO_2 after loading test were significantly greater than before. However, there was no significant difference in VOI without TACT (P value = 0.345). A.U.: arbitrary unit; N.S.: not significant.

In addition, we evaluated the effective slice-thickness of our system using a chart, which is a specially designed apparatus for the measurement of tomographic slice-thickness. This chart was placed at an angle $11°32'$ relative to the tomographic plane. Six concentric projections of chart images were obtained and reconstructed as a tomogram using the TACT program. Slice-thickness property was visually evaluated by one of the authors.

2.6 *Statistical Methods*

The Wilcoxon signed-rank test was used to assess differences in VOI and SpO_2 before and after a loading test. Multiple linear regression analysis was used to assess the relation between the current supplied to the LED and the signal intensity of the NIR images.

3 Results

Our system was capable of acquiring several projections for the tomograms within a few seconds in thick regions that cannot transmit [Fig. 2(a)] and easily reconstructs a tomogram using the TACT program [Fig. 2(b)].

VOI was good correlated with SpO_2 in this system during the loading test using a blood pressure cuff (Fig. 4). Both VOI with TACT and SpO_2 after the loading test were significantly lower than those before the loading test (P value = 0.0431, P value = 0.0431), but VOI without TACT showed no significant difference (P value = 0.345 (Fig. 5).

There was a high correlation between the signal intensity of NIR images and the current supplied to the LED at each wavelength in Fig. 6 ($R^2 = 0.998$, P value < 0.001 in 700 nm, $R^2 = 0.999$, P value < 0.001 in 810 nm). The effective slice-thickness of our system was 0.4 mm [Fig. 7(b)].

4 Discussion

A transmitted beam is generally used for NIR imaging,[8,9] but this system would obtain NIR images in thick regions that cannot transmit [Fig. 2(a)]. Some methods to obtain tomograms using NIR are reported,[21,22] but require lengthy imaging times, in the order of more than ten minutes, with the additional restraint of limited scan regions. We could obtain several projections for the tomograms within a few seconds and easily reconstruct a tomogram using TACT and even three-dimensional images [Figs. 2(b) and 2(c)]. TACT is usually used in an x-ray system

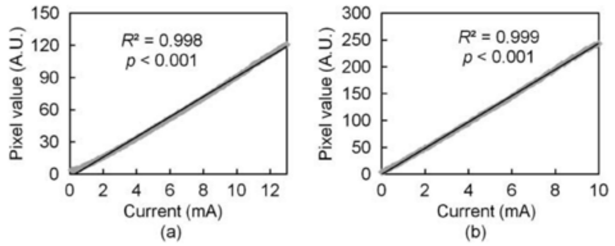

Fig. 6 Relationship between the signal intensity of NIR images and current (mA) in (a) 700 and (b) 810 nm LED. There was a high correlation between the signal intensity of NIR images and the current supplied to the LED at each wavelength. A.U.: arbitrary unit.

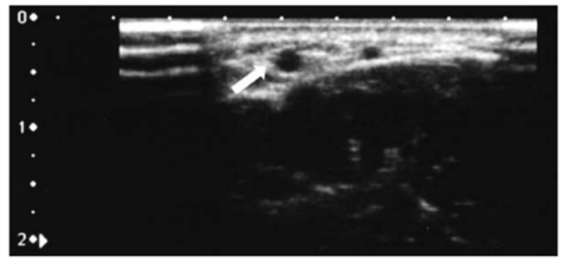

Fig. 8 Forearm surface vessels image by ultrasound. White arrow shows median antebrachial vein, which is 2.0 mm in diameter. Surface to vein distance is 5.0 mm.

(radiography is used as a basis image).[11–19] Although there has been no study that reconstructed NIR tomograms, the TACT reconstruction process in our system was a similar method to that in the x-ray system. Therefore, the number of projections needed to reconstruct the tomography, the accuracy of the method, and robustness of the method are not different between the x-ray system and our system.

VOI and SpO_2 demonstrated good correlation in this system (Fig. 4). The result indicates that we can evaluate oxygen saturation of surface vessels. After the cuff pressure was released, the VOI temporarily tended to rise compared to before the loading test. It is assumed that the blood flow volume temporarily increased as the blood flow was interrupted by the load and was rapidly effused when the cuff pressure was released. Moreover, measurement sensitivity was improved when tomograms were used for the calculation of VOI (Fig. 5), because tomograms can only evaluate the blood signals. However, the NIR image signal without TACT overlapped with the surrounding thick tissue signal. Although, at least six NIR images were required to reconstruct the tomograms, all images were acquired within one second. Thereby, temporary resolution is satisfied with the loading test for evaluating the oxygenation change. We used a pulse oximeter as the gold standard to measure SpO_2 and compared these findings with VOI, since it was desired to exclusively use noninvasive methods.

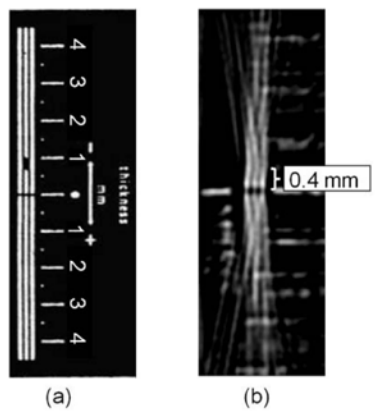

Fig. 7 (a) Picture of chart and (b) NIR image for assessing the slice thickness of NIR with TACT. Scale corresponding to the slice-thickness of the tomogram.

To analyze VOI, it is necessary that the relationship between NIR radiation and signal intensities of the images is linear, because signal intensity of an NIR image is relative value. In this study, there was a linear dependency between the current supplied to the LED and the image signal intensity (Fig. 6). Because it is already known that the relationship between the NIR signal intensity and current supplied to LED is linear,[23,24] linearity between NIR radiation and image signal intensities was verified by this study in the range where VOI was measured. Therefore, we can independently measure VOI of image signal intensity.

In tomosynthesis, slice-thickness is considered to be in relation to the angular disparity of the projection geometry, as in tomography. The effective slice-thickness of our system was 0.4 mm [Fig. 7(b)]. This was considered appropriate because forearm blood vessels used for the calculation of VOI were 2 mm in diameter (Fig. 8).

However, it must be noted that there are some variables in the measurement of VOI. First, the distance between the skin and CCD camera could have an impact on the acquired image data, because the focus of the lens mounted CCD camera of this system was matched to the surface vessels. Thus, NIR repeated scattering in air could be detected by the CCD camera, which might contribute to a decrease in image contrast. In the next series of studies, a grid will be attached, which is an optical fiber bundle, between the skin and CCD camera to decrease scattering effects. The different path lengths of the NIR transmitting subcutaneous tissue might cause different signal intensity attenuations. Therefore, an attenuation correction method by the analysis of skin tissues spatial fluorescence distribution by Monte Carlo simulation is required.[25,26] Additionally, to increase measurement precision of VOI, we need to establish a correction method of image inhomogeneous sensitivity at each wavelength.

We cannot show the advantage compared to the previous method on relevant NIR imaging, but it could enhance the proposed method, because, theoretically, the summation of images increases signal-to-noise ratio and image contrast of vessels compared with a single NIR image. Moreover, the ability to acquire three-dimensional spatial information would increase the diagnostically useful information available over that of a conventional two-dimensional display. Indeed, measurement sensitivity was improved when tomograms were used for the calculation of VOI. Of course, further clinically relevant investigations should be pursued in the future.

In future clinical works, we would like to apply our system to evaluate Reynaud's syndrome and torsion of the testis decreasing the regional vascular, tissue viability of skin grafts and bedsores, as well as skin inflammation due to breast radiation therapy.

5 Conclusion

This novel imaging system makes it possible to noninvasively obtain NIR tomograms containing three-dimensional information that can then be used to accurately analyze changes in oxygen saturation levels. There are several clinical applications for which this system will be best utilized, such as to increase treatment efficacy or to detect early symptoms of the adverse effects of radiation on the sensitive tissues of the skin. Further clinical studies are required to refine the system for everyday clinical usage.

References

1. M. Siegemund, J. Bommel, and C. Ince, "Assessment of regional tissue oxygenation," *Intensive Care Med.* **25**(10), 1044–1060 (1999).
2. S. Suzuki, S. Takasaki, T. Ozaki, and Y. Kobayashi, "A tissue oxygenation monitor using NIR spatially resolved spectroscopy," *Proc. SPIE* **3597**, 582–592 (1999).
3. D. A. Boas, T. Gaudette, G. Strangman, X. Cheng, J. J. Marota, and J. B. Mandeville, "The accuracy of near infrared spectroscopy and imaging during focal changes in cerebral hemodynamics," *Neuroimage* **13**(1), 76–90 (2001).
4. Y. Yoshitake, H. Ue, M. Miyazaki, and T. Moritani, "Assessment of lower-back muscle fatigue using electromyography, mechanomyography, and near-infrared spectroscopy," *Eur. J. Appl. Physiol.* **84**(3), 174–179 (2001).
5. A. Lima and J. Bakker, "Noninvasive monitoring of peripheral perfusion,"*Intensive Care Med.* **31**(10), 1316–1326 (2005).
6. W. A. Eaton, L. K. Hanson, P. J. Stephens, J. C. Sutherland, and J. B. R. Dunn, "Optical spectra of oxy- and deoxyhemoglobin," *J. Am. Chem. Soc.* **100**, 4991–5003 (1978).
7. H. D. Zeman, G. Lovhoiden, and C. Vrancken, "The clinical evaluation of vein contrast enhancement," in *Proc. 26th Ann. Int. Conf. IEEE Engineering in Medicine and Biology Society*, pp. 1203–1206 (2004).
8. M. Kono, H. Ueki, and S. Umemura, "Near-infrared finger vein patterns for personal identification," *Appl. Opt.* **41**(35), 7429–7436 (2002).
9. N. Miura, A. Nagasaka, and T. Miyatake, "Feature extraction of finger-vein patterns based on repeated line tracking and its application to personal identification," *Mach. Vision Appl.* **15**(4), 194–203 (2004).
10. S. J. Fearnley, "Pulse oximetry," *Update in Anaesthesia, Practical Procedures* **5**(2), 1 (1995).
11. R. L. Webber, R. A. Horton, D. A. Tyndall, and J. B. Ludlow, "Tuned-aperture computed tomography (TACT^{TM}). Theory and application for three-dimensional dento-alveolar imaging," *Dentomaxillofac Radiol.* **26**(1), 53–62 (1997).
12. R. L. Webber and W. Bettermann, "A method for correcting for errors produced by variable magnification in three-dimensional tuned aperture computed tomography," *Dentomaxillofac Radiol.* **28**(5), 305–310 (1999).
13. M. Abreu, Jr., D. A. Tyndall, J. B. Ludlow, and C. J. Nortjé, "The effect of the number of iterative restorations on tuned aperture computed tomography for approximal caries detection," *Dentomaxillofac Radiol.* **30**(1), 325–329 (2001).
14. M. K. Nair, H. G. Gröndahl, R. L. Webber, U. P. Nair, and J. A. Wallace, "Effect of iterative restoration on the detection of artificially induced vertical radicular fractures by tuned aperture computed tomography," *Oral Surg. Oral Med. Oral Pathol. Oral Radiol. Endod.* **96**(1), 118–125 (2003).
15. R. L. Webber, H. R. Underhill, and R. I. Freimanis, "A controlled evaluation of tuned-aperture computed tomography applied to digital spot mammography," *J. Digit Imaging* **13**(2), 90–97 (2000).
16. K. Yamamoto, Y. Hayakawa, Y. Kousuge, M. Wakoh, H. Sekiguchi, M. Yakushiji, and A. G. Farman, "Diagnostic value of tuned-aperture computed tomography versus conventional dentoalveolar imaging in assessment of impacted teeth," *Oral Surg. Oral Med. Oral Pathol. Oral Radiol. Endod.* **95**(1), 109–118 (2003).
17. K. Yamamoto, A. G. Farman, R. L. Webber, R. A. Horton, and K. Kuroyanagi, "Effects of projection geometry and number of projections on accuracy of depth discrimination with tuned-aperture computed tomography in dentistry," *Oral Surg. Oral Med. Oral Pathol. Oral Radiol. Endod.* **86**(1), 126–130 (1998).
18. K. Yamamoto, K. Nishikawa, N. Kobayashi, K. Kuroyanagi, and A. G. Farman, "Evaluation of tuned aperture computed tomography depth discrimination for image series acquired variously with linear horizontal, linear vertical and conical beam projection arrays," *Oral Surg. Oral Med. Oral Pathol. Oral Radiol. Endod.* **89**(6), 766–770 (2000).
19. A. G. Farman, J. P. Scheetz, P. D. Eleazer, M. J. Edge, L. Gettleman, R. D. Morant, S. Limrachtamorn, and K. Yamamoto, "Tuned-aperture computed tomography accuracy in tomosynthetic assessment for dental procedures," *International Congress Series* **126**, 695–699 (2001).
20. T. Ozawa, T. Saito, S. Numada, T. Nishiyasu, and N. Kondou, "Measurement of venous oxygen pressure by non invasive blood vessel monitor 'ASTRIM'," *Trans. Jpn. Soc. Med. Biol. Eng.* **40** (Suppl), 178 (2002).
21. D. M. Richter, "Computed tomography laser mammography, a practical review," *Nippon Igaku Hoshasen Gakkai Zasshi* **59**(6), 687–693 (2003).
22. X. Wang, D. L. Chamberland, P. L. Carson, J. B. Fowlkers, R. O. Bude, D. A. Jamadar, and B. J. Roessler, "Imaging of joints with laser-based photoacoustic tomography: an animal study," *Med. Phys.* **33**(8), 2691–2697 (2006).
23. Optrans, available at http://www.optrans.com/pdf/220-LSF811C1.PDF, Accessed 7 December (2010).
24. Optrans, available at http://www.optrans.com/pdf/217-VSF706C1.PDF, Accessed 7 December (2010).
25. D. Y. Churmakov, I. V. Meglinski, S. A. Piletsky, and D. A. Greenhalgh, "Analysis of skin tissues spatial fluorescence distribution by the Monte Carlo simulation," *J. Phys. D: Appl. Phys.* **36**, 1722–1728 (2003).
26. I. V. Meglinski and S. J. Matcher, "Computer simulation of the skin reflectance spectra," *Comput. Methods Programs Biomed.* **70**(2), 179–186 (2003).

[Original Article]

Simultaneous R_2^* and Liver Fat-fraction Measurement Using Modulus and Real Multiple Gradient-echo with Low-field MRI

Tatsuhiko MATSUSHITA[†,††], Tosiaki MIYATI[†,††], Naoki OHNO[†,†††], Tetsuo OGINO[†], Tomoyuki OKUAKI[†], Norio HAYASHI[†††], Akihiro KITANAKA[†], Takashi HAMAGUCHI[†††], Shigeki OHTAKE[†,††]

[†]Division of Health Science, Graduate School of Medical Science, Kanazawa University, 5-11-80 Kodatsuno, Kanazawa, 920-0942, Japan

[††]Wellness Promotion Science Center, Institute of Medical, Pharmaceutical and Health Science, Kanazawa University, 5-11-80 Kodatsuno, Kanazawa, 920-0942, Japan

[†††]Department of Radiology, Kanazawa University Hospital, 13-1 Takara-machi, Kanazawa, 920-8641, Japan

(Received on September 12, 2011. In final form on October 31, 2011)

Abstract : We evaluated the R_2^* (iron content) and fat-fraction of liver tissue simultaneously using the modulus and real multiple gradient-echo (MRM-GRE) sequence at low-field MRI. Using a 0.4-Tesla open MRI, modulus images of 4 gradient-echoes (typically 8.9, 17.8, 26.7, and 35.6 ms) were obtained by MRM-GRE. The real part of the first echo image was also reconstructed to differentiate below and above the 50 percent fat-fraction. R_2^* and the fat-fraction were obtained from the parameters of a theoretically fitted formula for each echo signal. R_2^* and fat-fraction were measured with MRM-GRE from phantom data, liver of healthy volunteers (n=12) and from patients with fatty liver (n=3). The phantom MRI-derived fat-fraction was in good agreement with the actual value, with R_2^* showing a strongly positive correlation to actual iron content. MRI-derived fat-fraction in fatty liver was higher than that in the volunteer. However, no significant difference in R_2^* was found between fatty liver and volunteers. These results show that MRM-GRE enables a method to differentiate causes of signal reduction whether due to an increasing R_2^* or increasing fat-fraction. MRM-GRE enables a simple and accurate assessment of fat and iron content at low-fields.

Key words : magnetic resonance imaging (MRI), R_2^*, fat-fraction, gradient echo (GRE), liver

1. Introduction

Reports on the role of imaging in the assessment of liver disease continue to gain in clinical importance [1]. The most frequently used modalities for liver imaging are ultrasonography, computed tomography and magnetic resonance imaging (MRI). Of these three techniques, MRI is a clinically powerful technique that is well recognized for its ability to depict and characterize disease of the liver [2]. MRI has been proposed for non-invasive detection and quantification of liver status [3]. Two useful methods, R_2^* and fat-fraction analysis, have been reported for evaluating liver status using MRI [4-12]. R_2^* analysis was found useful in evaluating liver iron concentrations such as in increasing iron contents (e.g. hemochromatosis or hemosiderosis) [4-5]. Fat-fraction analysis was often useful in the evaluation of liver tissue [8-12]. We reported on a useful fat-fraction analysis method based on the Dixon method, that is, the modulus and real multiple gradient-echo (MRM-GRE) method [13-15]. Using MRM-GRE, R_2^* and fat-fraction are simultaneously obtained. Moreover, this method can distinguish above and below the 50% fat-fraction. The T_2^*-iterative decomposition of water/fat using echo asymmetry and least-squares estimation (IDEAL) [16] is also especially useful for assessment when there is co-occurrence of hepatic steatosis and iron deposition (e.g. non-alcoholic hepatitis) [17-19]. However, these methods have been used with high-field MRI systems, but more than 15% of MRI systems in the world are low-field. Therefore, to expand the method to lower field strength, we evaluated liver tissue metabolism with a low-field MRI system. In this paper, we describe its characteristics, and demonstrate the utility of MRM-GRE.

2. Methods and Materials

2.1 R_2^* and fat-fraction analysis

First, four multiple echo modulus images, including first opposed-phase and in-phase images, were acquired using multiple echo GRE sequence. A real image was also obtained at the first opposed-phase echo to differentiate above and below 50% fat-fraction. Next, signal intensities from each obtained echo images were measured and fitted with a theoretical equation (Marquardt-Levenberg algorithm) [20]. The signal from a voxel containing water and fat can be written as [21] :

$$I_t = \{|I_{w0}|^2 + |I_{f0}|^2 + 2|I_{w0}||I_{f0}|\cos\Delta\omega t\}^{1/2} \exp(-t/T_2^*) \qquad (1)$$

where I_t is total signal intensity, I_{w0} and I_{f0} are initial water and fat signal intensities, $\Delta\omega$ is the frequency difference between water and fat. In equation (1), T_2^* of water and fat are combined. In addition, since equation (1) contains the T_2^* decay term and the phase difference term between water and fat, the initial signal intensities of water and fat obtained by fitting are without the influence of T_2^* decay and phase cycling [21]. Finally, R_2^* $(=1/T_2^*)$ were directly obtained from the parameters of a formula theoretically fitted with each echo signal, and the fat-fraction was calculated by substituting the initial signal intensities into equation (2).

$$\textit{Fat-fraction}\,(\%) = 100\, I_{f0}/(I_{w0}+I_{f0}) \qquad (2)$$

Then, using the real image obtained in the first opposed-phase echo, fat-fractions of below and above 50% were determined by the signs of signal intensities from this real component. A real positive component implied the signal intensities of water were larger than those of fat; therefore, the fat-fraction was determined as below 50%. Likewise, when the real component was negative, signified the signal intensities of water were smaller than those of fat; therefore, the fat-fraction was determined as above 50%.

2.2 *In Vitro* Phantom Study

2.2.1 Phantoms

Fat-Water (iron) phantoms consisting of bottles (approximately 200 mL) filled with equal volumes of distilled water and triglyceride (lard) were used to test the MRM-GRE method quantitatively. Aliquots of superparamagnetic iron oxide (SPIO) (Feridex, Bayer healthcare) were added to the vials to shorten T_2^* values in varying iron concentrations (0.05, 0.2, 0.4, 0.6, and 0.8 mM). In this scene, water and lard were separated in two layers, because of differences of specific gravities between water and lard. To vary the fat-fraction by using partial volume effect, the slice level which was oriented parallel to water-lard boundary was moved up and down. Additionally, to evaluate the state of emulsion, mayonnaises of 38.3% and 79.2% fat-fraction were measured.

2.2.2 Phantom Imaging

Imaging was performed with a 0.4-T open MRI system (APERTO Eterna; Hitachi Medical Corporation, Japan). For imaging, phantoms were individually fixed in an acrylic container filled with deionized water to avoid susceptibility artifacts caused by air around the phantoms. The phantoms were positioned centrally in a QD Head coil. After performing three plane localizing sequences, MRM-GRE scan was performed. Imaging parameters included 150 ms repetition time (TR), 4.4, 8.9, 13.3, and 17.8 ms echo time (TE), 40 mm section thickness to minimize the effect of imperfect slice profiles, single section acquired, 256 mm field of view (FOV), 256 × 256 matrix, ± 100 kHz bandwidth (BW) for reducing water-fat shift, ten number of signal averages to improve the signal-to-noise ratio, rephasing gradient off, and low flip angle (12°) was used to minimize T_1 effects [22-23].

Fat-fraction using MRM-GRE was compared to fat-fraction using Double-GRE Dixon method. Fat-fraction using Double-GRE Dixon method was obtained using equation (3, 4 and 5).

$$I_{in}=I_w+I_f, \quad (3)$$

$$I_{opp}=I_w-I_f, \quad (4)$$

$$Fat\text{-}fraction\,(\%)=100(I_{in}-I_{opp})/2\,I_{in}, \quad (5)$$

where, I_{in} and I_{opp} are in-phase and opposed-phase signal intensities, and I_w and I_f are water and fat signal intensities. Imaging parameters used were the same scan parameters as in MRM-GRE scans except for TE, i.e., 8.9 and 17.8 ms TE.

2.3 *In Vivo* Human Study

2.3.1 Subjects

This study was approved by the institutional review board of Kanazawa University and informed consent was obtained from each participant. Twelve healthy volunteers [mean age, 23.2; standard deviation (SD), 2.7 years; range 21-29; twelve men] and three patients diagnosed with fatty liver [mean age, 34.3; SD, 12.7 years; range 26-49; three men] were included in the study. The diagnosis of fatty liver was established as hyper-echogenicity of liver relative to kidney on ultrasound scanning. We measured the fat–fraction at the right lobe of the liver.

2.3.2 Human Imaging and MR Spectroscopy

Imaging was performed with a 0.4-T open MRI system with a QD Flexible Body coil. Each participant was placed in the supine position. MRM-GRE scan of the liver was performed in the axial plane using the scan parameters modified from those for phantom scans (150 ms TR, 8.9, 17.8, 25.6, and 35.6 ms TE, 10 mm section thickness, 11 mm interval, three sections acquired, 340 × 272 mm rectangular FOV, 240 × 102 matrix, ± 30 kHz BW, one number of signal averages, 17 seconds scan times) to adjust scan times within a single breath–hold period.

In typical clinical cases, single voxel breath-hold MR Spectroscopy (MRS) data was acquired to provide a reference standard from two patients with fatty liver [mean age, 38.5; SD, 16.3 years; range 26-49]. MRS was performed with a 3.0-T MRI (Signal HDx, GE Healthcare, Waukesha, WI) using phased array TORSO coil. Spectra were acquired using point-resolved spectroscopy without water suppression. A 3.0 × 3.0 × 3.0 cm^3 MRS voxel was placed in the same attempted location for MRM-GRE scan while avoiding large vessels, but without references to MRS including the following: 1500 ms TR, one number of signal averages. T_2 corrections were performed during postprocessing, 25, 45, 65, 85, 135, 185, 235, and 285 ms TE were acquired, within single 15 s breath hold. MRS spectra were postprocessed using spectroscopy analysis from General Electric (SAGE) to integrate the area under the water peak (4.7 ppm) and total area under the fat peaks (1.3 ppm), to obtain MRS fat–fraction.

3. Results

3.1 *In Vitro* Phantom Study

R_2^* value of the phantom showed a strongly positive correlation with the actual iron content (R^2=0.998 and P value < 0.001 in 0% fat-fraction, R^2=0.981 and P value < 0.001 in 10% fat-fraction, R^2=0.989 and P value < 0.001 in 30% fat-fraction; multiple linear regression analysis) (Fig.1).

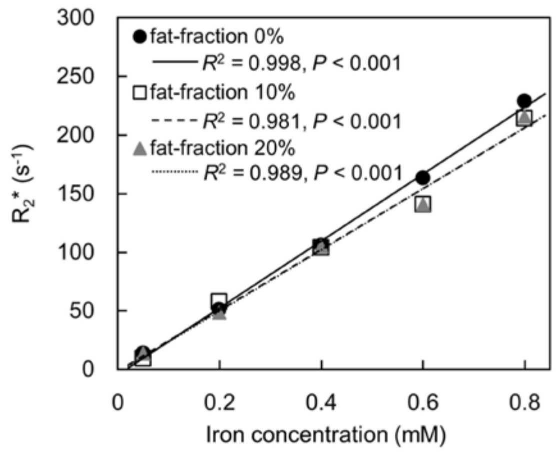

Fig.1 Relationship between phantom R_2^* and iron concentration. A strong positive correlation exists between R_2^* and iron concentration.

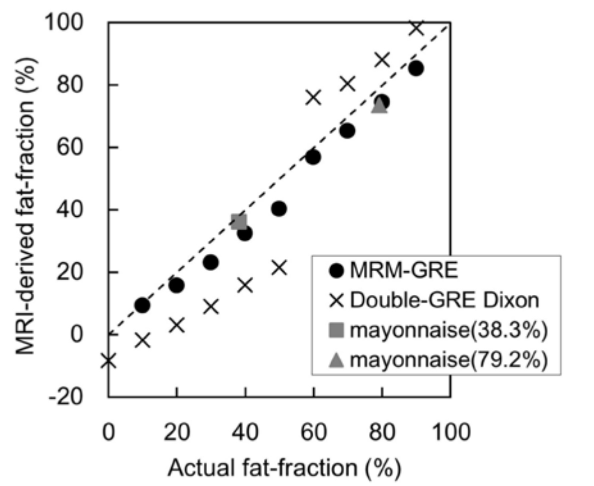

Fig.2 Relationship between phantom MRI-derived and actual fat-fraction. Double-GRE Dixon method yielded overestimations under conditions of high fat content and underestimations in low fat-fractions, whereas MRI-derived fat-fraction using T_2^* decay correction with MRM-GRE signals corresponded with the actual fat-fraction. Dashed line represents unity.

Fat-fractions using MRM-GRE with phantoms and mayonnaises were in good agreement with the actual value; however, fat-fraction using Double-GRE Dixon with phantom was either underestimated (< 50%) or overestimated (> 50%) (Fig.2).

3.2 *In Vivo* Human Study

Fig.3 illustrates the influence of fat-fraction on iron concentration of the liver. There was no significant correlation between R_2^* and fat content of the liver (R^2=0.040 and P value=0.531; multiple linear regression analysis) (Fig.3).The fat-fractions using Double-GRE Dixon were quite smaller than those with MRM-GRE (Fig.4(a)), and the fat-fractions using MRM-GRE in fatty liver were in good agreed with those using 3.0-T MRS (Fig.4(b)).

4. Discussion

Utility of R_2^* and fat-fraction analysis have been reported for evaluating the condition of liver using high-field MRI system [4-12]; however, these methods were not established in low-field conditions. The T_2^*-IDEAL [16] is also especially useful in the assessment when there is co-occurrence of hepatic steatosis and iron deposition (e.g. non-alcoholic hepatitis), but this method is not necessarily implemented in standard MR imagers. Therefore, we evaluated R_2^* and fat-fraction analysis of the liver using MRM-GRE at low-field MRI system.

The phantom study demonstrated a strong positive correlation between R_2^* and iron concentration (Fig.1). This result implies that the assessment of liver iron concentration could be directly obtained from the R_2^* value. As shown in the methods section 2.1, we could correct for T_2^* decay and phase cycling using MRM-GRE, as we obtained the initial water and fat signal fitted by equation (1), which contains the T_2^* decay term and the phase difference term between water and fat. Therefore, MRI-derived fat-fractions using MRM-GRE method were in good agreement with the actual fat-fractions. In addition, MRI-derived fat-fractions of mayonnaises corresponded with the actual fat-fraction. This also confirms that MRM-GRE method can be as effective in emulsions. On the other hand, the fat-fractions using Double-GRE Dixon method were affected by both T_2^* decay and phase cycling. The fat-fractions using Double-GRE Dixon were either underestimated (< 50%) or

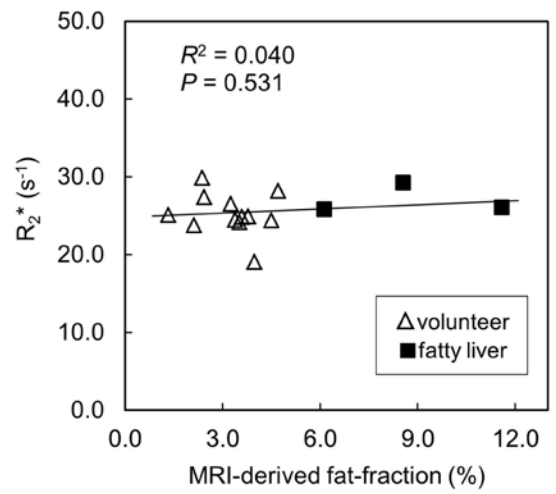

Fig.3 Relationship between human R_2^* and MRI-derived fat-fraction. There was no significant correlation between R_2^* and fat content of the liver.

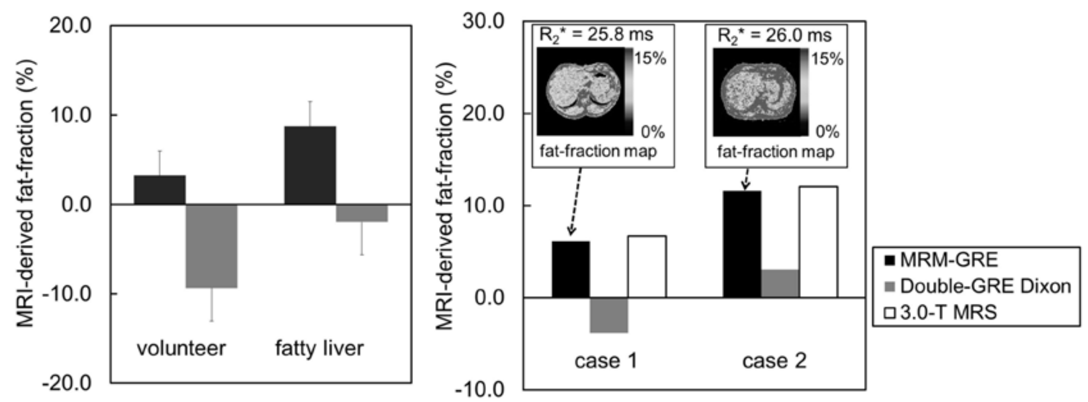

Fig.4 (a) Comparison of MRM-GRE and Double-GRE Dixon with human imaging. The fat-fractions using Double-GRE Dixon were smaller than those with MRM-GRE. (b) Typical cases with fatty liver comparison among MRM-GRE, Double-GRE Dixon, and 3.0-T MRS. MRI-derived fat-fraction using MRM-GRE in fatty liver agreed with those using 3.0-T MRS.

overestimated (> 50%), because of T_2^* decay and phase cycling (Fig.2).

The human studies showed no significant correlation between R_2^* and fat content of the liver (Fig.3). This result implies that assessment of iron concentration of the liver is unaffected by differences in fat content. The fat-fractions using Double-GRE Dixon were quite smaller than those with MRM-GRE due to T_2^* decay and phase cycling (Fig.4(a)). Additionally, the fat-fractions using MRM-GRE in typical cases with fatty liver were in good agreement with those using 3.0-T MRS (Fig.4(b)). MRM-GRE at low magnetic field strengths could be an effective clinical tool as a consequence of these results.

Fat suppression techniques are commonly used in MR imaging and are required in many clinical situations. However, since chemical-shift between water and fat is relatively small in low static field, frequency-selective fat suppression [24-25] or binominal pulse techniques [26] have difficulty in suppressing fat signals. The MRM-GRE method makes it possible to simply obtain the water and fat signal. MRM-GRE method can also measure T_2^* relaxation time. Accordingly, MRM-GRE method is an effective water-fat separation (i.e. fat-suppression) and T_2^* decay correction technique at low static magnetic field strength.

5. Conclusion

It was possible to simultaneously acquire measurements of R_2^* and fat-fraction using MRM-GRE at low-field MRI. A linear dependency between R_2^* and iron concentration, and MRI-derived fat-fraction using MRM-GRE method was in good agreement with actual values. MRM-GRE method makes it possible to simply and accurately assess iron and fat contents with low-field MRI. The ability to obtain both values at the same time allows one to optimize the advantages of each and obtain more information regarding liver metabolism at low static magnetic field strength.

References

[1] Hamer OW, Schlottmann K, Sirlin CB, et al.: Technology insight: advances in liver imaging, Nat Clin Pract Gastroenterol Hepatol, 4(4), 215-228, 2007.

[2] Low RN: Abdominal MRI advances in the detection of liver tumours and characterization, Lancet Oncol, 8(6), 525-535, 2007.

[3] Gandon Y, Olivié D, Guyader D, et al.: Non-invasive assessment of hepatic iron stores by MRI, Lancet, 31 (363), 357-362, 2004.

[4] Chappell KE, Patel N, Gatehouse PD, et al.: Magnetic resonance imaging of the liver with ultrashort TE (UTE) pulse sequences, J Magn Reson Imaging, 18(6), 709-713, 2003.

[5] Wood JC, Enriquez C, Ghugre N, et al.: MRI R^2 and R_2^* mapping accurately estimates hepatic iron concentration in transfusion-dependent thalassemia and sickle cell disease patients, Blood, 106(4), 1460-1465, 2005.

[6] Storey P, Thompson AA, Carqueville CL, et al.: R_2^* imaging of transfusional iron burden at 3T and comparison with 1.5T. J Magn Reson Imaging, 25, 540-547, 2007.

[7] Hankins JS, McCarville MB, Loeffler RB, et al.: R_2^* magnetic resonance imaging of the liver in patients with iron overload, Blood, 113(20), 4853-4855, 2009.

[8] Qayyum A, Goh JS, Kakar S, et al.: Accuracy of liver fat quantification at MR imaging: comparison of out-of-phase gradient-echo and fat-saturated fast spin-echo techniques-initial experience, Radiology, 237(2), 507-511, 2005.

[9] Hussain HK, Chenevert TL, Londy FJ, et al.: Hepatic fat fraction: MR imaging for quantitative measurement and display-early experience, Radiology, 237(3), 1048-1055, 2005.

[10] Cotler SJ, Guzman G, Layden-Almer J, et al.: Measurement of liver fat content using selective saturation at 3.0 T, J Magn Reson Imaging, 25(4), 743-748, 2007.

[11] Schuchmann S, Weigel C, Albrecht L, et at.: Non-invasive quantification of hepatic fat fraction by fast 1.0, 1.5 and 3.0 T MR imaging, Eur J Radiol, 62(3), 416-422, 2007.

[12] Johnson NA, Walton DW, Sachinwalla T, et al.: Noninvasive assessment of hepatic lipid composition: Advancing understanding and management of fatty liver disorders, Hepatology, 47(5), 1513-1523, 2008.

[13] Matsunaga S, Miyati T, Onoguchi M, et al.: Dual-Double-gradient-echo MRI for Liver Fat Content Analysis, Medical Imaging and Information Sciences, 23(1), 8-10, 2006.

[14] Ohno N, Miyati T, Ono E, et al.: Simultaneous R_2^* and fat fraction determination of the liver with modulus and real multiple gradient-echo MRI, In: Proceedings 17th Scientific Meeting, International Society for Magnetic Resonance in Medicine, Honolulu, Hawaii, 4089, 2009.

[15] Motono Y, Miyati T, Ueda Y, et al.: Simultaneous analysis of marrow fat fraction and bone mineral density with modulus and real multiple gradient-echo MRI, Medical Imaging and Information Sciences, 27(1), 14-17, 2010.

[16] Yu H, McKenzie CA, Shimakawa A, et al.: Multiecho reconstruction for simultaneous water-fat decomposition and T_2^* estimation, J Magn Reson Imaging, 26(4), 1153-1161, 2007.

[17] George DK, Goldwurm S, MacDonald GA, et al.: Increased hepatic iron concentration in nonalcoholic steatohepatitis is associated with increased fibrosis, Gastroenterology, 114(2), 311-3118, 1998.

[18] Tomita K, Tanimoto A, Irie R, et al.: Evaluating the severity of nonalcoholic steatohepatitis with superparamagnetic iron oxide-enhanced magnetic resonance imaging, J Magn Reson Imaging, 28(6), 1444-1450, 2008.

[19] Mitsuyoshi H, Yasui K, Harano Y, et al.: Analysis of hepatic genes involved in the metabolism of fatty acids and iron in nonalcoholic fatty liver disease, Hepatol Res, 39(4), 366-373, 2009.

[20] Marquardt DW: An algorithm for least-squares estimation of nonlinear parameters, J Soc Indust Appl Math, 11(2), 431-441, 1963.

[21] Parizel PM, Van Riet B, van Hasselt BA, et al.: Influence of magnetic field strength on T_2^* decay and phase effects in gradient echo MRI of vertebral bone marrow, J Comput Assist Tomogr, 19(3), 465-471, 1995.

[22] Liu CY, McKenzie CA, Yu H, et al.: Fat quantification with IDEAL gradient echo imaging: correction of bias from T 1 and noise, Magn Reson Med, 58(2), 354-364, 2007.

[23] Yokoo T, Bydder M, Hamilton G, et al.; Nonalcoholic fatty liver disease: diagnostic and fat-grading accuracy of low-flip-angle multiecho gradient-recalled-echo MR imaging at 1.5 T, Radiology, 251(1), 67-76, 2009.

[24] Haase A, Frahm J, Hänicke W, et al.: 1H NMR chemical shift selective (CHESS) imaging, Phys Med Biol, 30(4), 341-344, 1985.

[25] Kaldoudi E, Williams SC, Barker GJ, et al.: A chemical shift selective inversion recovery sequence for fat-suppressed MRI: theory and experimental validation, Magn Reson Imaging, 11(3), 341-355, 1993.

[26] Hore PJ: A new method for water suppression in the proton NMR spectra of aqueous solutions, J Magn Reson, 54, 539-542, 1983.